Galindo, J.; Dolz, V.; Tiseira, A.; Ponce-Mora, A. (2021). Numerical assessment of the dynamic behavior of a solar-driven jet-ejector refrigeration system equipped with an adjustable jet-ejector. International Journal of Refrigeration. 121:168-182. https://doi.org/10.1016/j.ijrefrig.2020.10.019

NUMERICAL ASSESSMENT OF THE DYNAMIC BEHAVIOUR OF A SOLAR-DRIVEN JET-EJECTOR REFRIGERATION SYSTEM EQUIPPED WITH AN ADJUSTABLE JET-EJECTOR

Authors

José Galindo, Vicente Dolz [1], Andrés Tiseira, Alberto Ponce-Mora

Abstract

The present paper compares numerically the mid-term performance of two different architectures of a solar-driven jet-ejector refrigeration system: The first one is fitted with a fixed-geometry jet-ejector while the second one is equipped with an adjustable spindle that modifies the jet-ejector area ratio. The jet-ejector behavior has been predicted with a validated CFD approach and the dynamic response of the overall system accounts for transient effects in a small parabolic trough collector and a hot thermal storage tank. The investigation shows that the adjustable jet-ejector allows for continuous and smooth operation in a much wider range of outdoor conditions. Additionally, it enables more efficient management of the thermal level in the hot storage system. As a result, the adjustable refrigeration system improves the performance indicators in all the warm months of the typical meteorological year under evaluation. The maximum improvement potential is found in May; the fixed-geometry system provides an average COP_{th} of 0.34 while the adjustable system reaches an average COP_{th} of 0.48 considering the same boundary conditions in both cases.

Keywords

Solar cooling, Jet-ejector refrigeration, Environmentally friendly refrigerants, Energy efficiency, Adjustable jet-ejector, Dynamic behavior

Nomenclature

Acronyms

AJE	Adjustable Jet-Ejector
AJERS	Adjustable Jet-Ejector Refrigeration System
AR	Jet-ejector area ratio
CFD	Computational Fluid Dynamics
COP	Coefficient Of Performance
DNI	Direct Normal Irradiation
FJE	Fixed-geometry Jet-Ejector
FJERS	Fixed-geometry Jet-Ejector Refrigeration System
GWP	Global Warming Potential
HTF	Heat Transfer Fluid
ODP	Ozone Depletion Potential
PTC	Parabolic Trough Collector

[1]Corresponding Author: Vicente Dolz, CMT – Motores Térmicos, Universitat Politècnica de València, 46022, Spain. Telf: (+34) 963 877 650, Email: vidolrui@mot.upv.es

SP	Spindle Position
TMY	Typical Meteorological Year
TSS	Thermal Storage System

Notation

Latin

A	Area [m^2]
k	Thermal conductivity [$W \cdot m^{-1} \cdot K^{-1}$]
h	Specific enthalpy [$J \cdot kg^{-1}$]
$\dot{m}$	Mass flow rate [$kg \cdot s^{-1}$]
P	Pressure [bar]
$\dot{Q}$	Heat exchanger power [W]
T	Temperature [$°C$]
V	Volume [m^3]

Greek letters

α	Angle [°]
η	Efficiency [-]
ρ	Density [$kg \cdot m^{-3}$]
ω	Jet-ejector entrainment ratio [-]

Subscripts

acc	Accumulation term
abs	Absorber
amb	Ambient
adv	Advection term
cl	Cooling load
co	Condenser/Condensing conditions
col	Solar collector
cond	Conduction term
conv	Convection term
e	Jet-ejector
ev	Evaporator
gc	Glass cover
ge	Generator
HTF	Heat Transfer Fluid
in	Inlet
loss	Thermal losses
mf	Jet-ejector mixed flow
mw	Mineral wool layer
opt	Optical
out	Outlet
pf	Jet-ejector primary flow
rad	Radiation term
ref	Reference situation/condition

sf	Jet-ejector secondary flow
ste	Steel layer
sol	Solar
th	Thermal
TSS	Thermal Storage System

1. INTRODUCTION

The limited market penetration of jet-ejector refrigeration technologies is partly due to the inability of a particular jet-ejector design to show a robust performance when either the design cooling load, the outdoor conditions, or the heat source thermal level are altered (Omidvar et al., 2016). The reference operating conditions for which the jet-ejector is designed exercise a decisive influence on its performance and a jet-ejector with a fixed geometry suffers a severe performance degradation away from its design region.

Technical solutions based on mechanical actuators exist to tackle this issue at the expense of increasing the mechanical complexity of the refrigeration system. Two adaptation mechanisms have attracted most of the research efforts: (i) Parallel multi-ejector systems composed by multiple jet-ejectors with different scales or geometric configurations in which a particular design comes into operation depending on the boundary conditions (Besagni et al., 2016; Chen et al., 2015, 2013), (ii) Variable geometry jet-ejectors in which mechanical actuators are intended to allow continuous and precise tuning of one or more jet-ejector dimensions (Chen et al., 2019, 2017a; Lin et al., 2012; Liu et al., 2012; Pereira et al., 2014). The latter has gained great interest thanks to its flexibility and its superior performance when adapting to multiple operating conditions. Owing to manufacturing limitations in real systems the vast majority of adjustable jet-ejector arrangements consist of a needle moving axially to open or close the jet-ejector primary nozzle throat (Chen et al., 2017b; Pereira et al., 2014). In this manner, the jet-ejector area ratio (ratio between the mixing chamber area and the primary nozzle throat area) can be varied. To a lesser extent, some authors also considered jet-ejector layouts with a variable nozzle exit position (NXP) (Hu et al., 2014; Wang et al., 2018) or even multiple mechanical degrees of freedom and active solutions that can be altered simultaneously (Chen et al., 2019; Wang et al., 2018).

Within the jet-ejector refrigeration systems intended for solar cooling applications, the aforementioned off-design problem becomes more important due to the fluctuating nature of climatic conditions and solar irradiation availability. Bearing that in mind, the dynamic response of the baseline refrigeration system layout has been analyzed in the literature following both a numerical (Allouche et al., 2017; Diaconu et al., 2011; Tashtoush et al., 2015) and an experimental approach (Pollerberg et al., 2009; Varga et al., 2017) to acquire a broader perspective on the system's feasibility. Normally, these basic arrangements lack active devices that modify the jet-ejector internal dimensions.

The feasibility of using adjustable jet-ejectors has been postulated in solar-driven refrigerations systems (Chen et al., 2017b; Dennis and Garzoli, 2011; Ma et al., 2010; Omidvar et al., 2016; Varga et al., 2013, 2011; Yen et al., 2013). However, the improvement potential offered by an adjustable jet-ejector geometry in comparison with the traditional approach that is, a fixed configuration, has not been assessed in detail during the warm months of a typical meteorological year (mid-term period).

The main innovative aspect of the present investigation is the comparison of a solar-assisted jet-ejector refrigeration system with two different architectures working under the dynamic conditions imposed by the solar irradiation and ambient temperature evolution. The first one corresponds to the conventional layout with a fixed-geometry jet-ejector. The second one implements an adjustable jet-ejector in which the jet-ejector area ratio can be actively controlled by using a movable spindle. To do so, the transient response of the solar field side has been taken into account by considering a dynamic model of a real parabolic trough collector and a thermal storage system. Both configurations have been assessed by considering the climatic conditions of a warm Mediterranean region with extensive air-conditioning requirements during summer periods.

The main objectives of the present research paper can be summarized as follows:

- To characterize numerically the operating envelope of an adjustable jet-ejector.
- To evaluate numerically the feasibility of making use of a spindle to modify the jet-ejector primary nozzle throat area as a mechanism to improve the operational range of the refrigeration system when the ambient temperature changes.
- To compare the performance of a fixed and adjustable jet-ejector from the perspective of the overall refrigeration system efficiency considering a PTC as the collecting device and a hot thermal storage system.
- To analyze the dynamic response of the solar-driven jet-ejector refrigeration system considering the fluctuating nature of solar irradiation and outdoor conditions.

2. DEFINITION OF THE SOLAR-ASSISTED REFRIGERATION SYSTEM

Figure 1 shows the thermally-driven refrigeration system with its three main subsystems: the collecting device (parabolic trough collector), the thermal storage system and the jet-ejector refrigeration cycle. Two different jet-ejector arrangements have been considered for the jet-ejector refrigeration system. The first one corresponds with the traditional approach in which the jet-ejector internal geometry is designed for a reference operating condition and remains unchanged during service. The second one can actively modify the jet-ejector area ratio (AR) by using a spindle. It represents an advanced control strategy intended to gain versatility against variable operating conditions.

The environmentally friendly refrigerant R1234yf has been used as a working fluid due to its low ecological impact ($GWP = 4$, $ODP = 0$) and its favorable performance when utilized in solar-assisted jet-ejector refrigeration systems (Galindo et al., 2020).

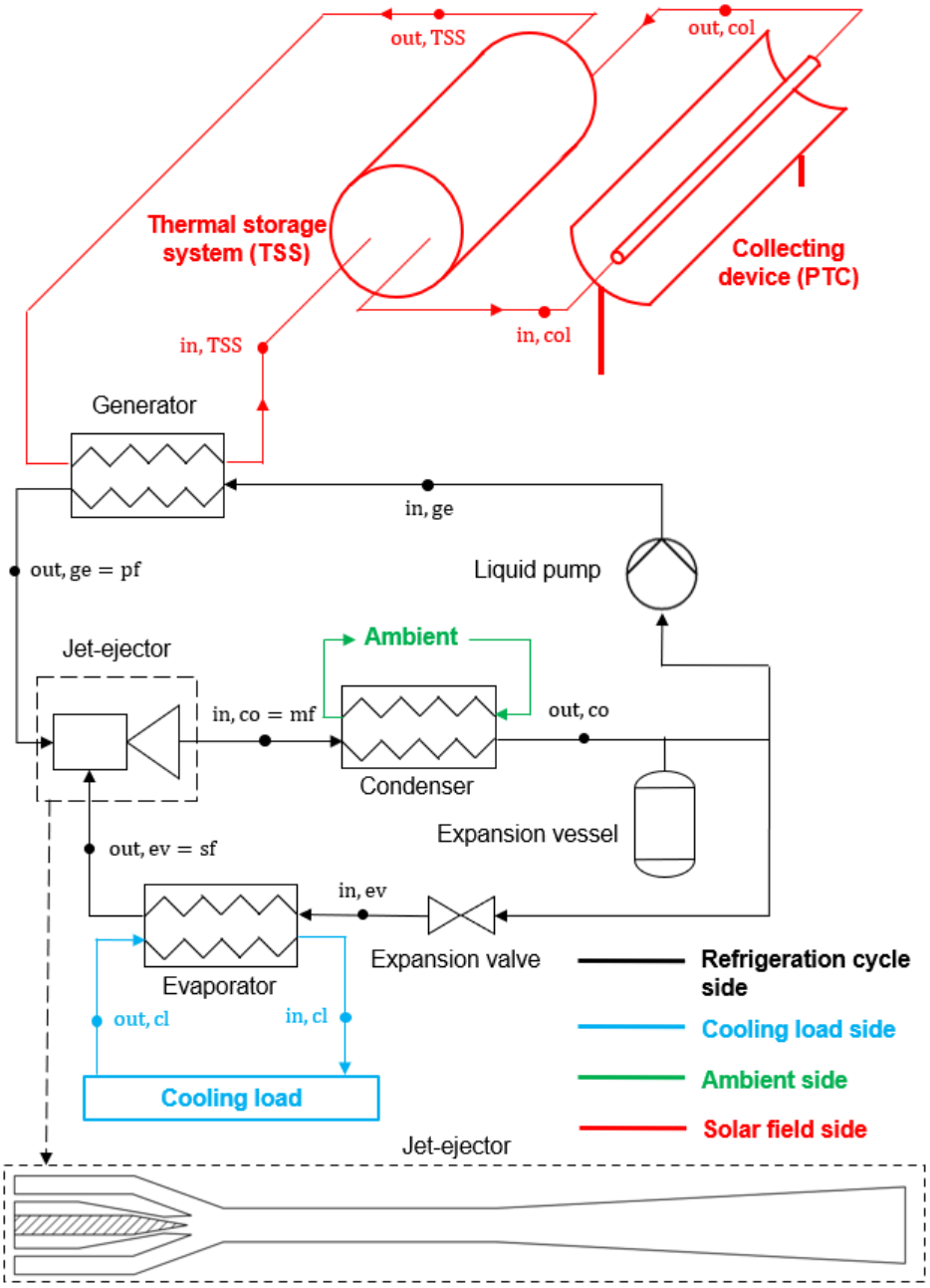

Figure 1. Solar-assisted jet-ejector refrigeration system with a thermal storage tank

2.1 Fixed-geometry jet-ejector refrigeration system

The fixed-geometry jet-ejector refrigeration system (FJERS) is equipped with a fixed jet-ejector (FJE) in which the movable spindle is fixed in a reference position. For this reference location the jet-ejector primary nozzle outlet diameter ($D_{e,1}$), the mixing chamber diameter ($D_{e,2}$) and the nozzle exit position ($L_{e,1}$) are optimized according to the reference operating conditions. Figure 2 illustrates the internal geometry of the FJE with its most relevant dimensions and Table 1 summarizes the main assumptions.

The definition of the reference operating conditions will have a strong influence on jet-ejector performance. An evaporating temperature of 13 °C which is consistent with the typical evaporating temperatures in air-conditioning applications has been selected (Gil and Kasperski, 2015; Varga et al., 2013). Assuming a pinch point of 7 °C an indoor temperature of 20 °C would be attainable. A reference condensing temperature of 31 °C, which is near the average daily maximum outdoor temperature in some Mediterranean latitudes, has been considered as a reference boundary condition. With the aforementioned pinch point and some degree of liquid subcooling, this ambient temperature would be compatible with a condensing temperature of 40 °C. This decision represents a trade-off and somewhat sacrifices the maximum achievable entrainment ratio in the double-choking mode for the sake of increasing the jet-ejector operative range.

The generating conditions are based in the study of Galindo et al. (Galindo et al., 2020) who carried out a sensitivity analysis of the generating temperature/pressure considering the same working fluid as well as the same reference evaporating and condensing conditions. The heat exchange process is assumed isobaric and the refrigerant leaves the generator at supercritical conditions ($P = 35.1\ bar$ and $T = 101.1$ °C).

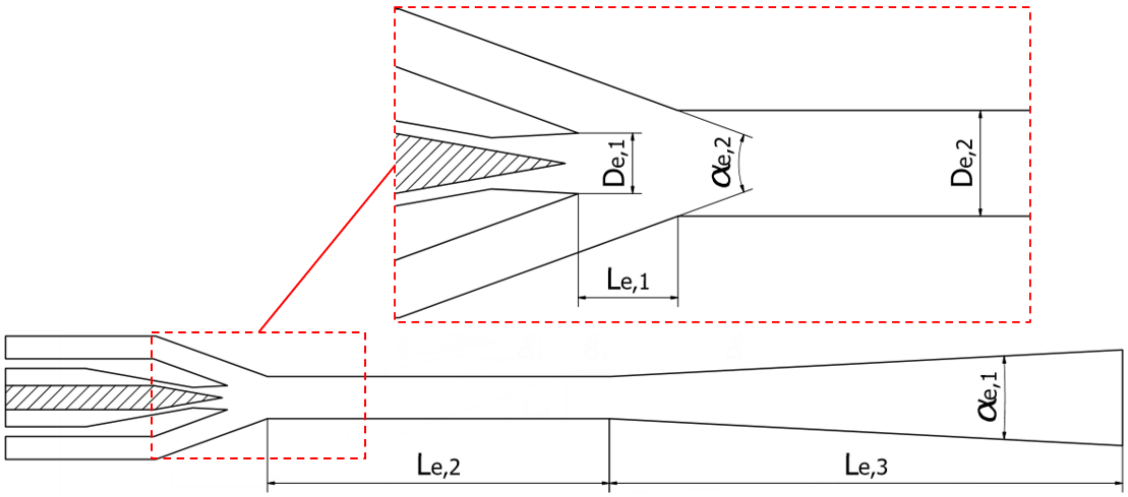

Figure 2. General and detailed view of the FJE (fixed spindle) and the AJE (movable spindle)

Dimension	Value
$\alpha_{e,1}[°]$	6
$\alpha_{e,2}[°]$	40
$L_{e,1}[\mathrm{mm}]$	Subject to optimization
$L_{e,2}[\mathrm{mm}]$	30
$L_{e,3}[\mathrm{mm}]$	45
$D_{e,1}[\mathrm{mm}]$	Subject to optimization
$D_{e,2}[\mathrm{mm}]$	Subject to optimization

Table 1. Main dimensions of the FJE

2.2 Adjustable jet-ejector refrigeration system

In the adjustable jet-ejector refrigeration system (AJERS) the jet-ejector arrangement is identical to the fixed configuration (see Figure 2) except for the spindle axial movement which is considered a mechanical degree of freedom. The adjustable jet-ejector (AJE) is intended to compensate variations in outdoor temperature assuming that the evaporating and generating conditions remain invariable throughout the system operation.

3. NUMERICAL MODELS

3.1 Jet-ejector CFD model

The jet-ejector entrainment ratio (Equation (1)) has been predicted for multiple geometric configurations and operating conditions by using a CFD code.

$$\omega = \frac{\dot{m}_{sf}}{\dot{m}_{pf}} \tag{1}$$

The CFD approach allows taking account of the jet-ejector internal geometry with a high level of detail. The CFD simulation framework reproduces the same setup described by Galindo et al. (Galindo et al., 2020). Two-dimensional, steady-state and compressible turbulent flow has been assumed as well as single-phase hypothesis in all the computational domain. For further details about the CFD configuration, the reader should refer to the aforementioned reference (Galindo et al., 2020). A computational mesh of approximately 50,000 elements has been considered representing a trade-off between precision and computational economy. It guarantees an accurate quantification of the jet-ejector global parameters. Indeed, the relative variations in the entrainment ratio do not exceed 1% if the computational mesh is further refined. For each spindle position of the AJE, the mesh has been adapted conveniently.

The thermodynamic properties of the working fluid under consideration (R1234yf) are dynamically loaded into the solver during the calculation thanks to an embedded model that accounts for real gas effects (Richter et al., 2011).

3.2 Jet-ejector refrigeration cycle

The jet-ejector refrigeration cycle model is based on energy and mass conservation in each element and uses the jet-ejector entrainment ratio provided by the CFD approach as input. The thermal power consumed from the TSS ($\dot{Q}_{ge}$), the cooling capacity ($\dot{Q}_{ev}$) and the COP_{th} are given as outputs (Equations (2), (3) and (4)) as a function of the condensing temperature and the spindle position. It must be noted that, as the condensing conditions change, the spindle movement in the adjustable jet-ejector (AJE) modifies the primary mass flow rate. This effect

varies the thermal power required by the refrigeration system and the resulting cooling capacity. To draw a fair comparison between both jet-ejector architectures it is assumed that the refrigeration system consumes 15 kW of thermal power when the cycle works at its reference condensing temperature (40 °C). For this rated thermal power the cooling capacity corresponds to 5.4 kW.

$$\dot{Q}_{ge} = \dot{m}_{pf} \cdot \left(h_{out,ge} - h_{in,ge}\right) \tag{2}$$

$$\dot{Q}_{ev} = \dot{m}_{sf} \cdot \left(h_{out,ev} - h_{in,ev}\right) \tag{3}$$

$$COP_{th} = \frac{\dot{Q}_{ev}}{\dot{Q}_{ge}} = \omega \cdot \frac{h_{out,ev} - h_{in,ev}}{h_{out,ge} - h_{in,ge}} \tag{4}$$

The previous mathematical expressions are computed ensuring that the pinch point temperature difference is met in all the heat exchangers.

3.3 PTC model

A Parabolic Trough Collector (PTC) with a span of 7.08 m, an aperture area of 5.76 m and a total collecting area of 40.78 m^2 has been chosen. The collecting device is equipped with a Schott PTR70 tube receiver with the same span. It is composed of an external glass cover, a vacuum film and a metal layer (absorber) containing the heat transfer fluid (Syltherm 800). Figure 3 shows a schematic view of the PTC and the layers composing the receiver tube. The numerical model implemented to predict the thermal behavior inside the lines of the PTC is based on the model proposed by Fasquelle et al. (Fasquelle et al., 2017) and Desideri et al. (Desideri et al., 2018), and accounts for the following heat transfer phenomena:

- Conduction along the axial direction in the heat transfer fluid, the absorber, and the glass cover ($\dot{Q}_{cond,HTF}$, $\dot{Q}_{cond,abs}$ and $\dot{Q}_{cond,gc}$).
- Convection between the heat transfer fluid and the absorber ($\dot{Q}_{conv,HTF\leftrightarrow abs}$).
- Radiation between the absorber and the glass cover ($\dot{Q}_{rad,abs\leftrightarrow gc}$).
- Convection between the glass cover and the ambient ($\dot{Q}_{conv,gc\leftrightarrow amb}$).
- Radiation between the glass cover and the ambient ($\dot{Q}_{rad,gc\leftrightarrow amb}$).

The energy balance for the elements that form the tube receiver, that is, the heat transfer fluid (Equation (5)), the absorber (Equation (6)) and the glass cover (Equation (7)) results in a set of partial differential equations that are discretized in nodes to find a numerical solution. The model is fed with specific hourly solar irradiation and ambient temperature data of Valencia Airport location ($\text{latitude} = 39.489°, \text{longitude} = 0.478°$). The dataset comes from the TMY computed in the time period 2006-2015 but the analysis is focused on the months with extensive air-conditioning utilization (April-September).

$$\dot{Q}_{acc,HTF} + \dot{Q}_{cond,HTF} + \dot{Q}_{conv,HTF\leftrightarrow abs} + \dot{Q}_{adv,HTF} = 0 \quad (5)$$

$$\dot{Q}_{acc,abs} + \dot{Q}_{sol,abs} + \dot{Q}_{cond,abs} + \dot{Q}_{conv,HTF\leftrightarrow abs} + \dot{Q}_{rad,abs\leftrightarrow gc} = 0 \quad (6)$$

$$\dot{Q}_{acc,gc} + \dot{Q}_{sol,gc} + \dot{Q}_{cond,gc} + \dot{Q}_{conv,gc\leftrightarrow amb} + \dot{Q}_{rad,gc\leftrightarrow amb} + \dot{Q}_{rad,abs\leftrightarrow gc} = 0 \quad (7)$$

Where the source term derived from the solar irradiation is shown in Equations (8) and (9):

$$\dot{Q}_{sol,abs} = DNI \cdot \eta_{opt,abs} \cdot A_{col} \quad (8)$$

$$\dot{Q}_{sol,gc} = DNI \cdot \eta_{opt,gc} \cdot A_{col} \quad (9)$$

The optical efficiency (η_{opt}) depends on the material transmittance, absorbance, and reflectivity as well as the incidence angle modifier obtained in optical qualification tests (Desideri et al., 2018). In the present model, it is assumed that a null angle of incidence can be attained with an adequate orientation and a sun-tracking system.

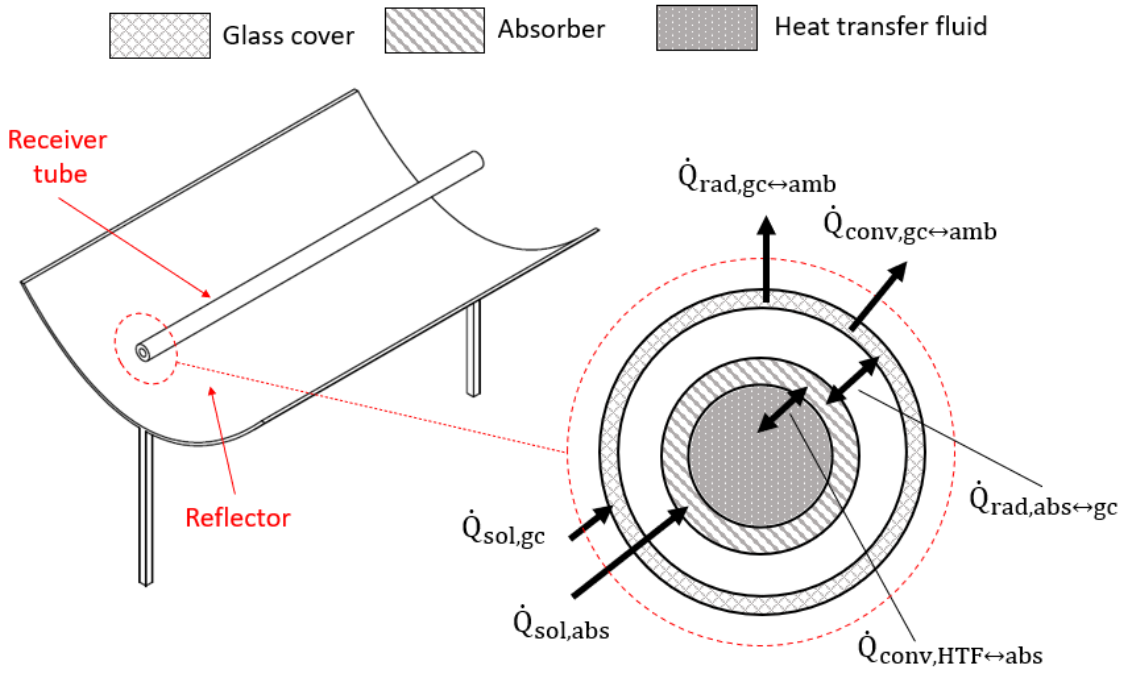

Figure 3. Schematic view of the parabolic trough collector (PTC) structure

3.4 Thermal storage system model

The Thermal Storage System (TSS) is conceived as a heat reservoir and it seeks to minimize the impact of intermittent heat supply caused by the unstable nature of climatic conditions. It has a cylindrical shape that minimizes its external area for a given volume. The TSS has been

dimensioned using as a guide the Spanish regulation applicable to solar facilities (Ministerio de Fomento (Gobierno de España), 2017; Rodríguez-Hidalgo et al., 2012):

$$0.05\ m < \frac{V_{TSS}}{A_{col}} < 0.18\ m \tag{10}$$

Considering this regulation, the lowest recommended ratio has been selected $\left(\frac{V_{TSS}}{A_{col}} = 0.05\ m\right)$ since priority is given to a rapid heating-up of the TSS after discharge events. This criterion gives a TSS volume of 2.04 m^3. The tank structure consists of three layers with a cylindrical shape (see Figure 4). The thermal and constructive properties of each layer are enumerated in Table 2.

Layer	Material	Thickness [cm]	k [$W \cdot m^{-1} \cdot K^{-1}$]
Internal (ste_1)	304 stainless steel	1	21
Intermediate (mw)	Mineral wool	3	0.04
External (ste_2)	304 stainless steel	1	21

Table 2. Thermal properties of the layers composing the TSS jacket

The following heat transfer phenomena have been considered to model the TSS thermal response (Zaversky et al., 2013):

- Natural convection between the heat transfer fluid and the internal steel layer ($\dot{Q}_{conv,TSS \leftrightarrow ste_1}$).
- Radiation between the heat transfer fluid and the internal steel layer ($\dot{Q}_{rad,TSS \leftrightarrow ste_1}$).
- Conduction through the internal steel later, the mineral wool layer and the external steel layer ($\dot{Q}_{cond,ste_1 \leftrightarrow mw}$ and $\dot{Q}_{cond,mw \leftrightarrow ste_2}$).
- Forced convection between the external steel layer and the ambient ($\dot{Q}_{conv,ste_2 \leftrightarrow amb}$).
- Radiation between the external steel layer and the ambient ($\dot{Q}_{rad,ste_2 \leftrightarrow amb}$).

Again, the energy balance for each TSS layer (Equations (11), (12), (13) and (14) results in a set of partial differential equations that are discretized in nodes to find a numerical solution

$$\dot{Q}_{acc,TSS} + \dot{Q}_{conv,TSS \leftrightarrow ste_1} + \dot{Q}_{ge} + \dot{Q}_{HTF} + \dot{Q}_{rad,TSS \leftrightarrow ste_1} = 0 \tag{11}$$

$$\dot{Q}_{acc,ste_1} + \dot{Q}_{conv,TSS \leftrightarrow ste_1} + \dot{Q}_{rad,TSS \leftrightarrow ste_1} + \dot{Q}_{cond,ste_1 \leftrightarrow mw} = 0 \tag{12}$$

$$\dot{Q}_{acc,mw} + \dot{Q}_{cond,ste_1 \leftrightarrow mw} + \dot{Q}_{cond,mw \leftrightarrow ste_2} = 0 \tag{13}$$

$$\dot{Q}_{acc,ste_2} + \dot{Q}_{cond,mw \leftrightarrow ste_2} + \dot{Q}_{rad,ste_2 \leftrightarrow amb} + \dot{Q}_{conv,ste_2 \leftrightarrow amb} = 0 \tag{14}$$

Where $\dot{Q}_{ge}$ is the thermal power extracted by the jet-ejector refrigeration system and $\dot{Q}_{HTF}$ refers to the thermal power input coming from the PTC (Equation (15)):

$$\dot{Q}_{HTF} = \dot{m}_{HTF} \cdot \left(h_{out,col} - h_{TSS}\right) \tag{15}$$

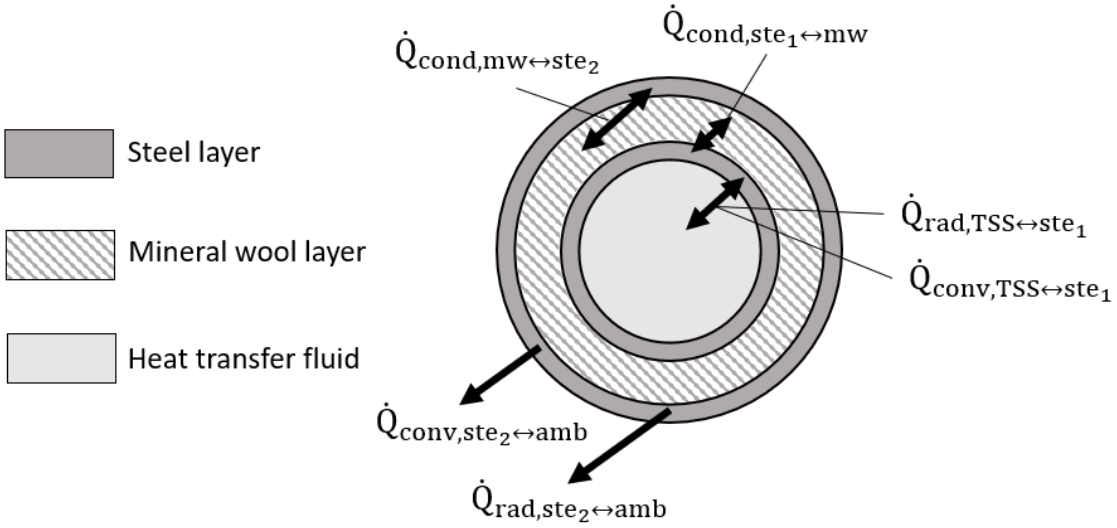

Figure 4. Cross-section of the cylindrical TSS

3.5 Integration of models and resolution scheme

The numerical models are linked together and interact as depicted in Figure 5. In the solar field side, the PTC is constantly recirculating thermal oil from the storage tank depending on the solar irradiation. The mass flow rate circulating through the PTC corresponds to its nominal value ($\dot{m}_{HTF} = 3\ \mathrm{kg \cdot s^{-1}}$) if the solar irradiation is greater than zero. In the absence of solar irradiation, the mass flow rate passing through the PTC is 50% of its nominal value if the hour under consideration is within the time-span 05:00-20:00 (this criterion assumes a temporary presence of clouds) and 10% of the nominal value otherwise (night period).

A simple control algorithm has been implemented to activate/deactivate the FJERS/AJERS depending on several variables being monitored instantaneously. Fundamentally, the refrigeration system is intended to be active every day in the time period comprising 08:00 to 19:00 if the ambient temperature is above 25 $°C$. If the PTC receives solar irradiation out of this time-span, as normally happens in the morning early hours, the resulting thermal power is dedicated to heating the TSS. Based on a pinch point analysis in the generator, the refrigeration system is switched on only if the temperature inside the TSS is above 120 $°C$. If the temperature of the TSS drops below the prescribed threshold during operation the refrigeration system switches off automatically to restore the minimum thermal level. On the contrary, if the TSS temperature exceeds 300 $°C$ the PTC is automatically defocused to avoid thermal degradation of the HTF.

According to the previous activation/deactivation criteria, the activation percentage can be defined as the ratio between the total time between 08:00 and 19:00 in which the ambient temperature is above $25°C$ and the refrigeration system is operating and the total time

comprised in the same interval in which the ambient temperature is above $25°C$. This ratio informs about the system's ability to be operative when there exist cooling needs.

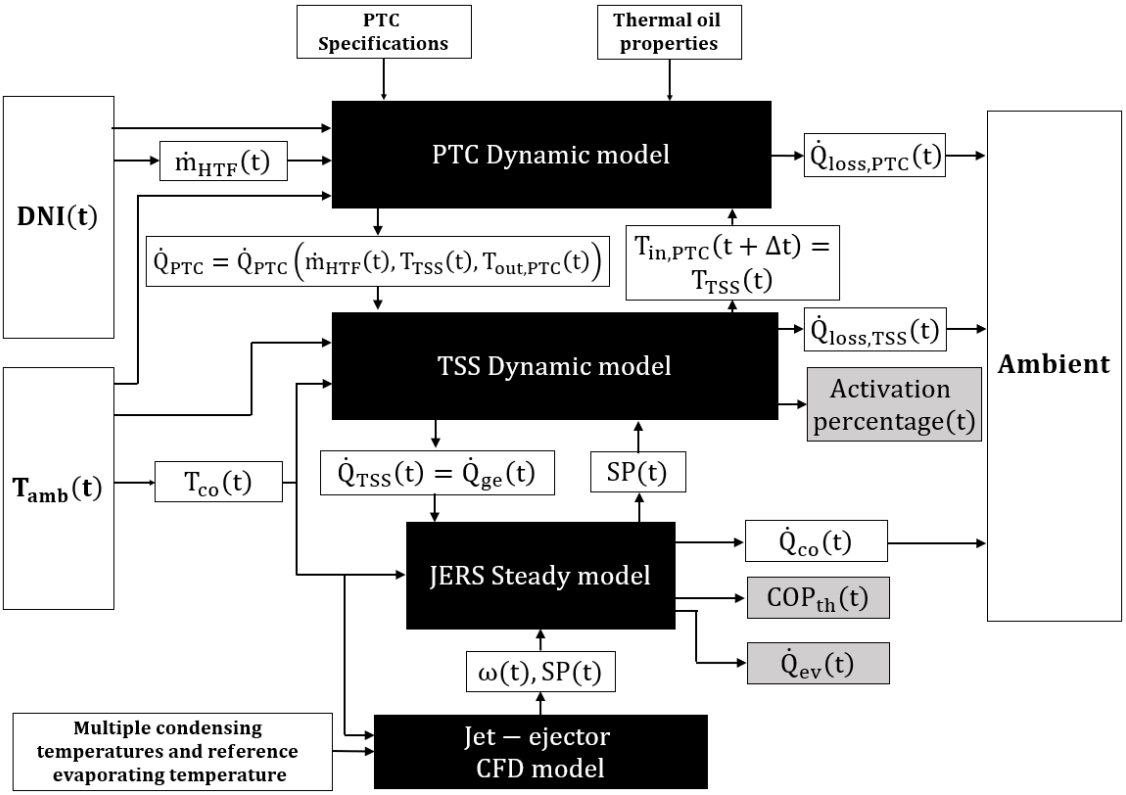

Figure 5. Interaction between all the models devoted to characterizing the refrigeration system dynamic response.

The resulting system of partial differential equations is discretized in nodes and resolved following an explicit scheme for the time discretization. The time step has been reduced to $\Delta t = 1$ s to guarantee numerical stability. It is assumed that the start-up of the thermally-driven refrigeration system occurs on the first day of each month at 00:00 and the initial temperature of all the components corresponds to the ambient temperature.

4. VALIDATION OF THE COMPUTATIONAL MODELS

4.1 Jet-ejector model

CFD models have been used in the present investigation to predict the jet-ejector entrainment ratio in multiple operating conditions and geometric configurations. To guarantee that the CFD approach is providing trustworthy results it has been validated using experimental research works (García Del Valle et al., 2014; Hakkaki-Fard et al., 2015a, 2015b). The "geometry A" of García del Valle et al. (García Del Valle et al., 2014) and the geometric configurations labeled as "EJECTOR I-III" by Hakkaki-Fard et al. (Hakkaki-Fard et al., 2015b, 2015a) have been reproduced to assess the accuracy of the CFD setup presented in subsection 3.1. Figure 6 compares the

entrainment ratio results predicted with the CFD code with the experimental results. The maximum relative error in the entrainment ratio between the computational and the experimental results is not exceeding 9.3% considering the experimental data of Hakkaki-Fard et al. and 9.5% when compared with the results of García del Valle et al. Hence, the present CFD approach constitutes an effective utility at modeling the jet-ejector response in a realistic way.

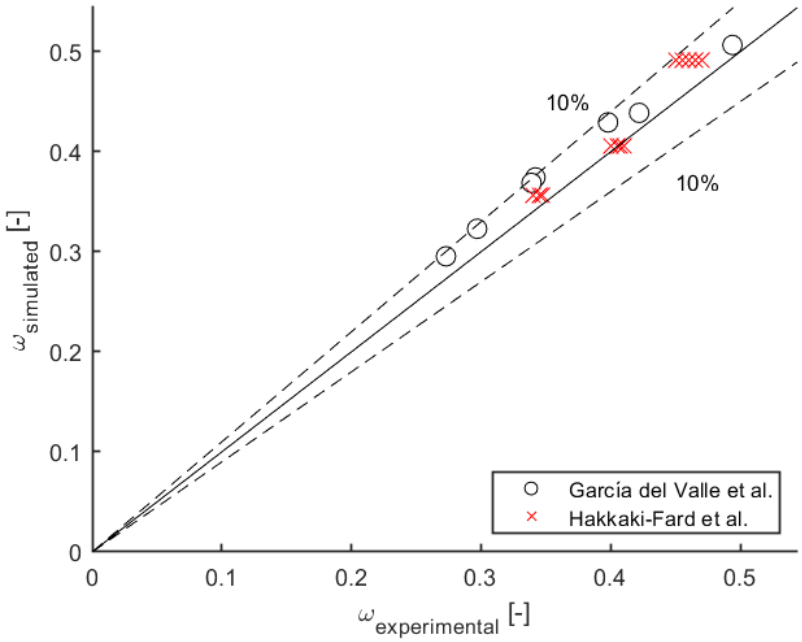

Figure 6. Experimental values of entrainment ratio vs entrainment ratio predicted with the present CFD approach

Typically, the CFD models simulating the transition between the jet-ejector double-choking and single-choking operating modes tend to overestimate the critical condensing temperature due to the effect of the surface roughness (Mazzelli and Milazzo, 2015). When the critical values predicted with the present CFD approach are compared to the experimental data of Shestopalov et al. (Shestopalov et al., 2015) the error in the critical condensing temperature is not exceeding 0.6 $°C$ for the three evaporating temperatures considered. Hence, the CFD code also represents a good approximation to reflect the FJE and the AJE performance in the single-choking operating mode.

4.2 PTC dynamic model

The nodal model of the PTC has been adjusted by using experimental data coming from a test campaign carried out at CIEMAT (Desideri et al., 2018). It must be outlined that the PTC used to adjust the nodal model has the same architecture and technical specifications as the prototype used in the present investigation being the only difference in the PTC total span. To assess the reliability of nodal model transient response it has been fed with the same record of instantaneous climatic parameters (solar irradiation, ambient temperature and incidence angle) and operational inputs (HTF mass flow rate, PTC inlet temperature and focusing-defocusing

patterns) registered during the experimental campaign. As can be observed in Figure 7 the nodal approximation of the PTC described in subsection 3.3 predicts precisely the evolution of the PTC outlet temperature.

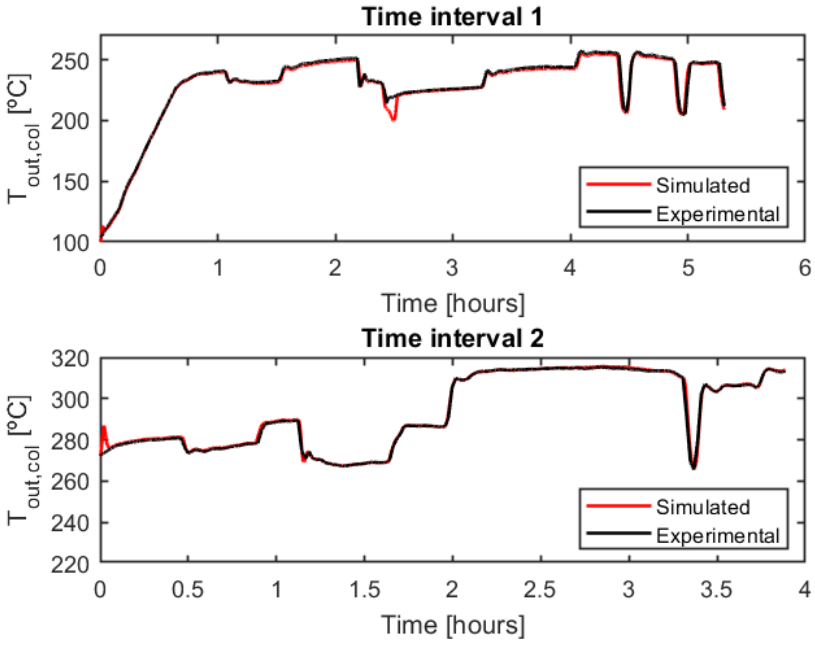

Figure 7. Temporal evolution of the PTC outlet temperature (simulated vs experimental)

5. RESULTS

5.1 Jet-ejector performance curves

Table 3 presents the optimum geometry of the FJE, which is scaled to meet the rated thermal power at the reference operating conditions ($T_{co} = 40°C$ and $T_{ev} = 13°C$).

Dimension	Value
$\alpha_{e,1}[°]$	6
$\alpha_{e,2}[°]$	40
$L_{e,1}[mm]$	6.5
$L_{e,2}[mm]$	55.4
$L_{e,3}[mm]$	83.2
$D_{e,1}[mm]$	3.9
$D_{e,2}[mm]$	6.8

Table 3. Optimized dimensions of the FJE

Having found the FJE optimum geometry, CFD simulations have been carried out to determine the jet-ejector critical operating temperature for multiple spindle positions. These simulations

are intended to characterize the performance envelope of the adjustable jet-ejector (AJE) and the fixed jet-ejector (FJE), in which the spindle remains fixed. The entrainment ratio results are depicted in Figure 8 for the AJE and three different geometries showing a fixed spindle position among which the reference FJE is included. The reference FJE has an $AR = 5.70$ (Figure 8) and in its double-choking operational mode, the entrainment ratio equals 0.40. It should be outlined that the operating envelope of the AJERS follows a linear trend.

As can be observed in Figure 8, moving the jet-ejector spindle upwards to increase the primary nozzle throat area is beneficial to increase the jet-ejector critical condensing temperature. Nevertheless, it reduces the jet-ejector entrainment ratio. Additionally, the increment in the nozzle throat effective area entails an increment of primary mass flow rate passing through it as depicted in Figure 9. The spindle displacement downwards causes the opposite effect, it reduces the critical condensing temperature positively affecting the jet-ejector entrainment ratio and diminishing the mass flow rate passing through the nozzle. These performance maps are used in the dynamic computational model that compares the FJERS and the AJERS and quantifies the potential improvement offered by the AJERS.

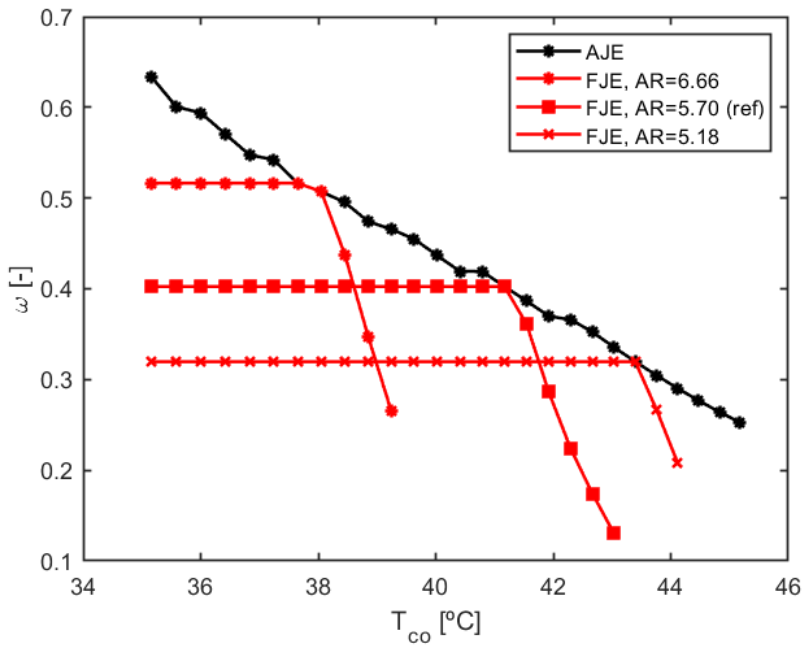

Figure 8. Entrainment ratio achievable for the FJE and the AJE versus condensing temperature

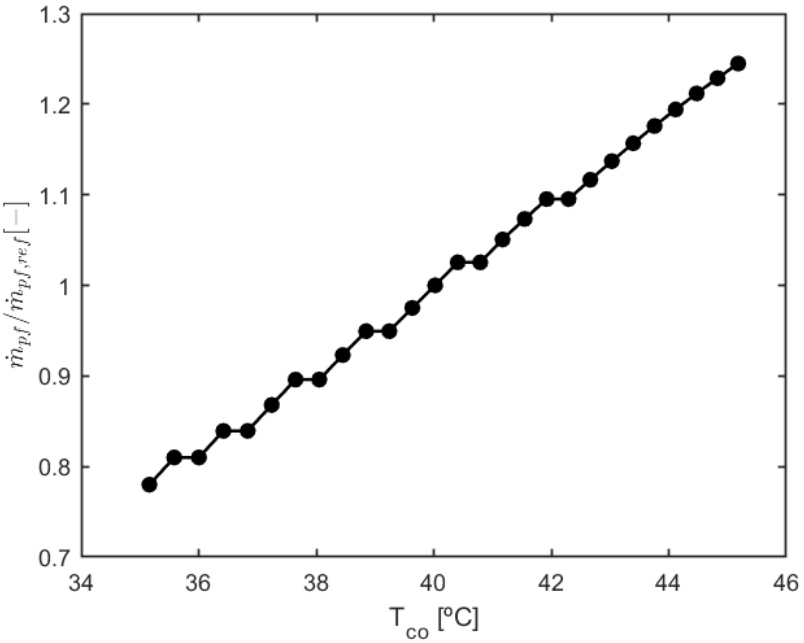

Figure 9. Primary mass flow rate versus condensing temperature for the AJE envelope. The results are non-dimensionalized with the reference FJE primary mass flow.

5.2 Transient behavior: comparison between the FJERS and the AJERS

5.2.1 Analysis of the reference month (July)

Two particular situations occurring in the reference month (July) have been analyzed to compare the dynamic behavior of the refrigeration system and its impact on cycle performance in both the FJERS and the AJERS. These specific events frequently occur considering a continuous operation during the warmer months of the year. The first one has a duration of three days and envisages the appearance of a partially cloudy day and the consequent lack of thermal level in the thermal storage system as depicted in Figure 10. The dashed lines delimit the hourly interval of interest (08:00-19:00) when computing the performance parameters. It is worth emphasizing that the ambient temperature in this interval is always below 31 $°C$, which is the reference ambient temperature for the FJERS. Under these circumstances, AJERS has great potential to improve the efficiency of the refrigeration system.

When either the FJERS or the AJERS are activated the rate of energy supply in the TSS is slightly greater than the rate of energy extracted towards the refrigeration system if the climatic conditions are favorable. Given this narrow margin, both refrigeration systems behave differently depending on their configuration. The AJERS required less thermal power coming from the TSS in the preceding hours and days to operate the refrigeration system. This fact is visible when T_{HTF} of both configurations are compared at the beginning of the first day (7th of July). Owing to this better management of the TSS thermal level, the heat reservoir is enough to face the temporary lack of solar irradiation occurring on the second day depicted in Figure 10. The instantaneous temperature in the TSS is all the time above the temperature defined as the threshold (120 $°C$). At the beginning of the third day, the thermal level of the TSS is still sufficient

to drive the AJERS despite the thermal losses to the ambient occurring during the night. Along these sample days, the AJERS is running the 100% of the time showing an average $COP_{th} = 0.50$. By contrast, the FJERS extracted more heat power from the heat reservoir in the preceding days so that it has a lower capacity to cope with the absence of solar irradiation in the early hours of the second day. When the low-temperature threshold is reached the control law deactivates the refrigeration system. This aims to restore rapidly the thermal level in the TSS with the hot flow coming from the PTC. The lack of available thermal power causes an irregular functioning of the refrigeration system leading to successive on and off sequences. The interruption harms the average COP_{th} and cooling capacity which is visible in Figure 10. The average COP_{th} equals 0.32 and the activation percentage reaches 95.3% in the time interval with cooling needs along the three sample days.

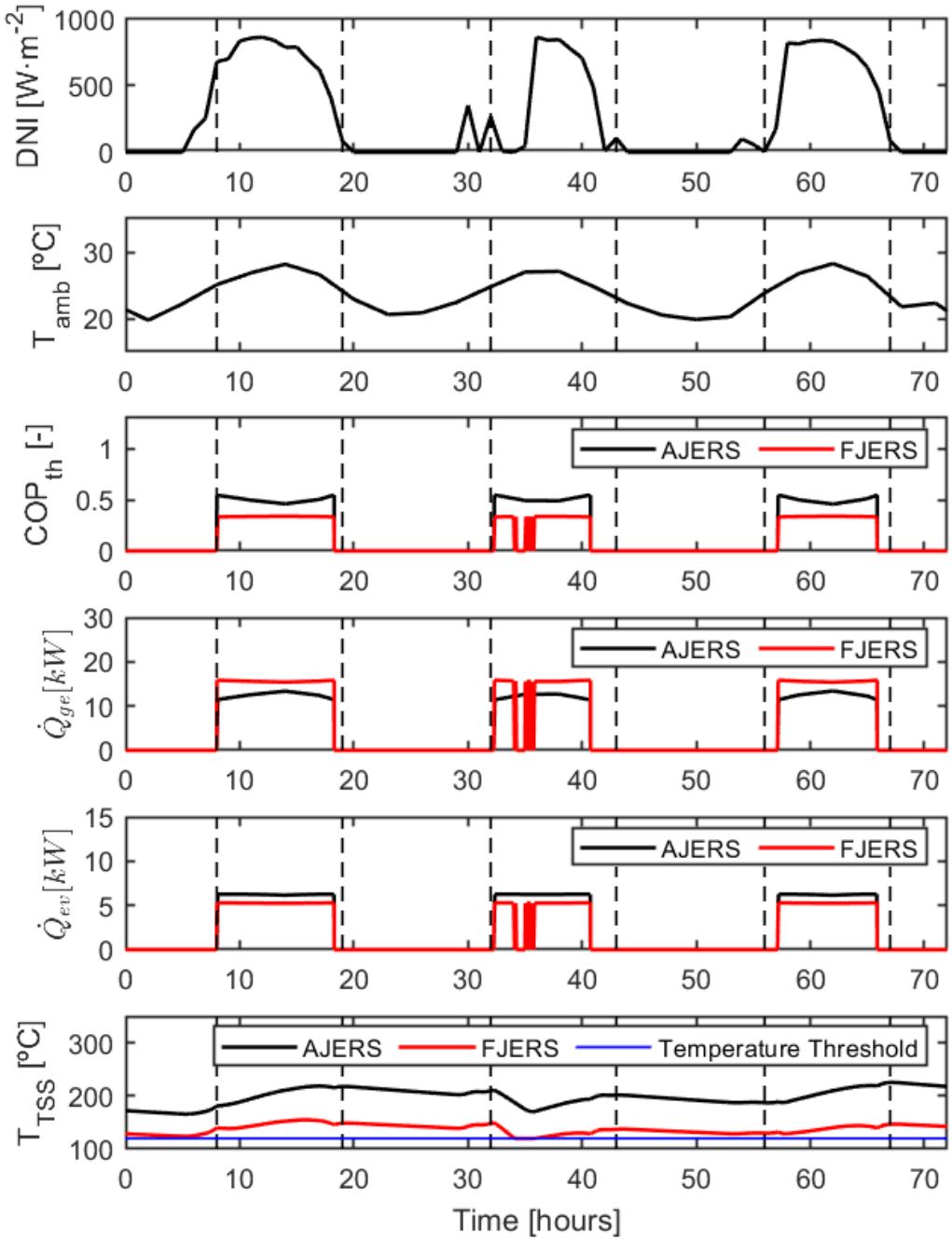

Figure 10. Instantaneous evolution of the main performance parameters of the refrigeration system: Case of study 1: 7th-9th of July.

The second scenario (see Figure 11) is characterized by an almost continuous solar irradiation supply which translates into a continuous operation along the five sample days. Indeed, both systems remain active 100% of the required period. The ambient temperature along these days, notwithstanding frequently exceeds the FJERS reference ambient temperature of 31 $°C$. This means that in the FJERS the jet-ejector might operate in the single-choking mode or even in its backflow mode in certain time slots with the consequent performance drop. The average COP_{th}

shown by the FJERS corresponds in this sample five days to 0.30. Conversely, the adaptation capability shown by the AJERS in this off-design scenario has a positive impact on the average efficiency, reaching a $COP_{th} = 0.40$. The unusually high temperatures occur in the 1st, 4th and 5th days.

As a general trend, it has been observed that the AJERS is an effective method to extend the operative range of the refrigeration system in the absence of solar irradiation as well as increasing the system performance. Its superior performance lies in the more efficient management of thermal energy available in the storage system when the operating conditions differ from the reference/design conditions. Indeed, when the analysis is extended to the overall month the AJERS exhibits superior average COP_{th} (0.42 versus 0.31) and activation percentage (96.5% versus 95.2%) when compared to the FJERS.

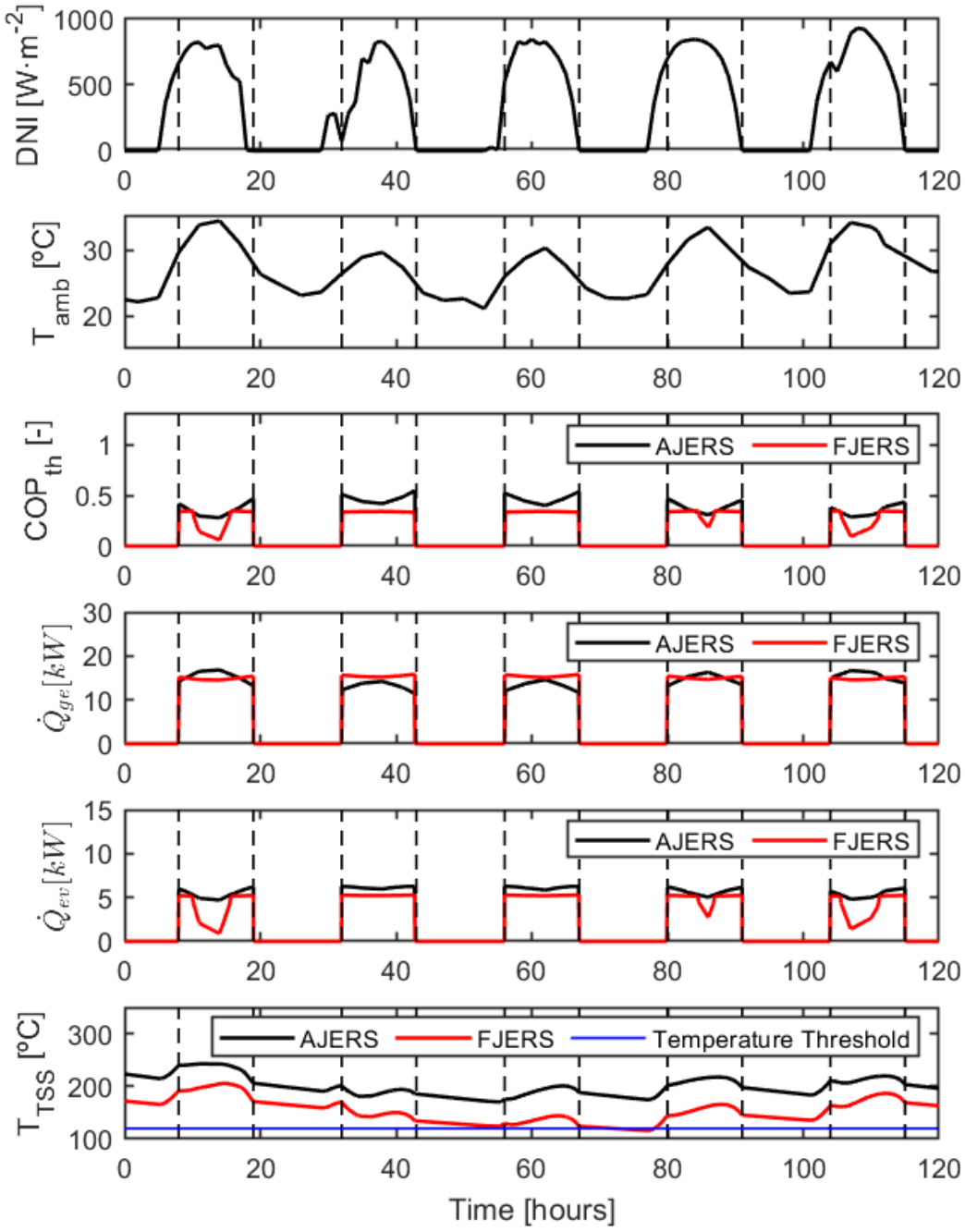

Figure 11. Instantaneous evolution of the main performance parameters of the refrigeration system: Case of study 2: 27th-31st of July.

5.2.2 Analysis extended to the rest of the warm months

The analysis of the monthly figures provides a comprehensive overview of the real improvement potential derived from the AJERS utilization. To do so, the instantaneous evolution of the main

performance indicators along the TMY months with frequent utilization of air-conditioning systems has been collected to present daily and monthly average figures. This exploration allows examining general trends more precisely.

The histogram plot of Figure 12 illustrates that the AJERS improves the FJERS efficiency irrespective of the month under consideration. To homogenize the representation of both configurations, ten levels of COP_{th} have been considered for each jet-ejector architecture to create the histogram except for May in which three levels are considered. This decision is sustained in the low dispersion of the results found in May. The FJERS has been designed to operate satisfactorily with an ambient temperature up to 31 $°C$, however, the appearance of more favorable outdoor conditions does not bring any benefit owing to the invariable response of the FJE when it works in the so-called double-choking operating mode. This establishes an upper limit in the maximum achievable COP_{th} for the FJERS. Taking the month of July as a representative sample it is observed that 25 days show a COP_{th} ranging between 0.31 and 0.35. Contrarily, the AJERS allows gradual adaptation to outdoor conditions and has a great potential for improving the jet-ejector entrainment ratio. It guarantees smooth operation and prevents the jet-ejector from functioning single-choking mode, where its performance is severely degraded. Indeed, in 5 days along this month, the AJERS operates with a COP_{th} ranging between 0.47 and 0.52.

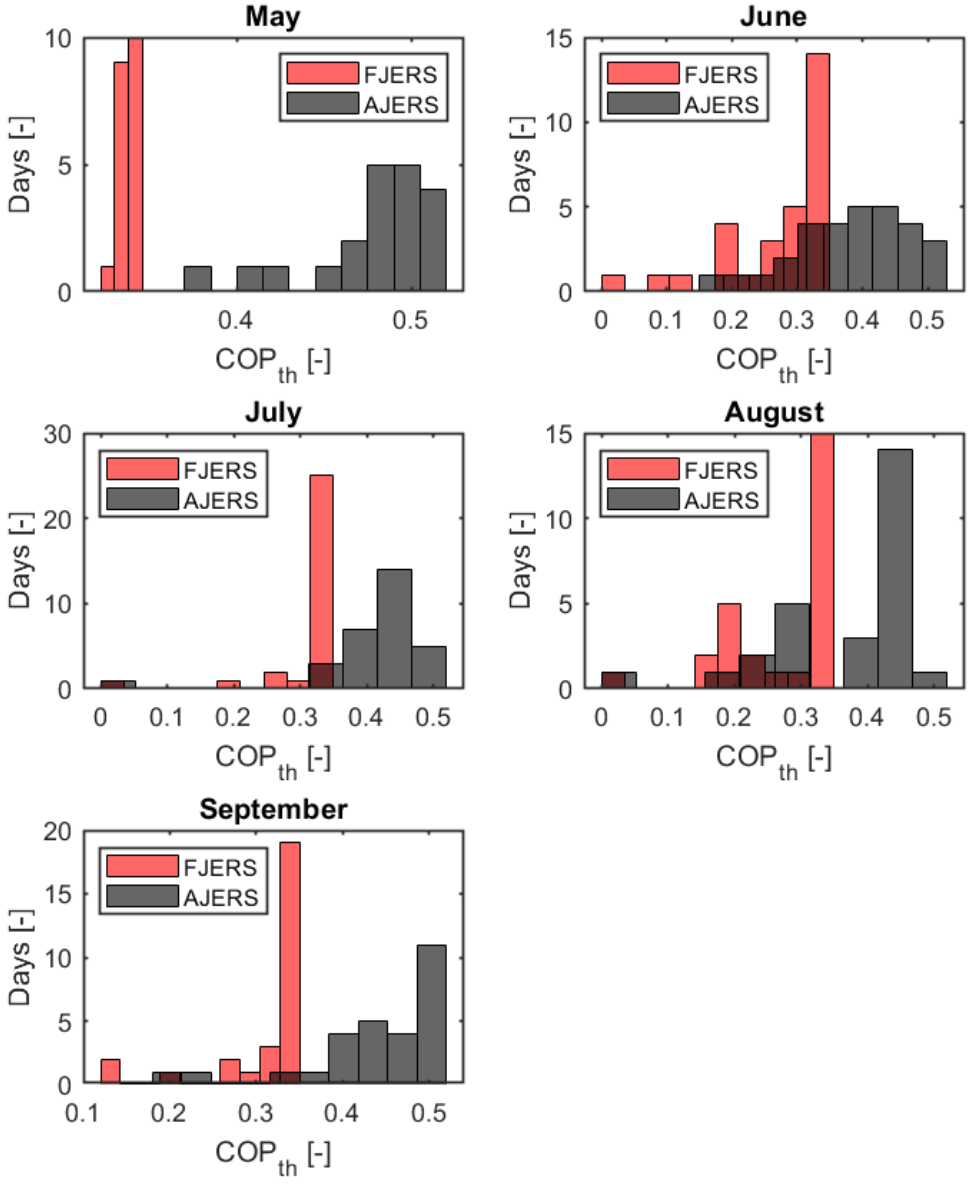

*Figure 12. Distribution of the daily average COP_{th} achieved by the FJERS and the AJERS along the warm months of the TMY. *Only the days with cooling needs have been represented: May (20 days), June (30 days), July (30 days), August (27 days), September (28 days).*

It must be outlined that the penalty caused by FJERS is more evident in those months with lower average ambient temperature, that is, May and September (Figure 13). In those months the average ambient temperature differs more from the FJERS design ambient temperature (31 °C) and the improvement potential offered by the AJERS is greater. The average AJERS COP_{th} in May and September corresponds to 0.48 and 0.44, respectively, while the FJERS reaches COP_{th} values of 0.34 and 0.31 considering the same months.

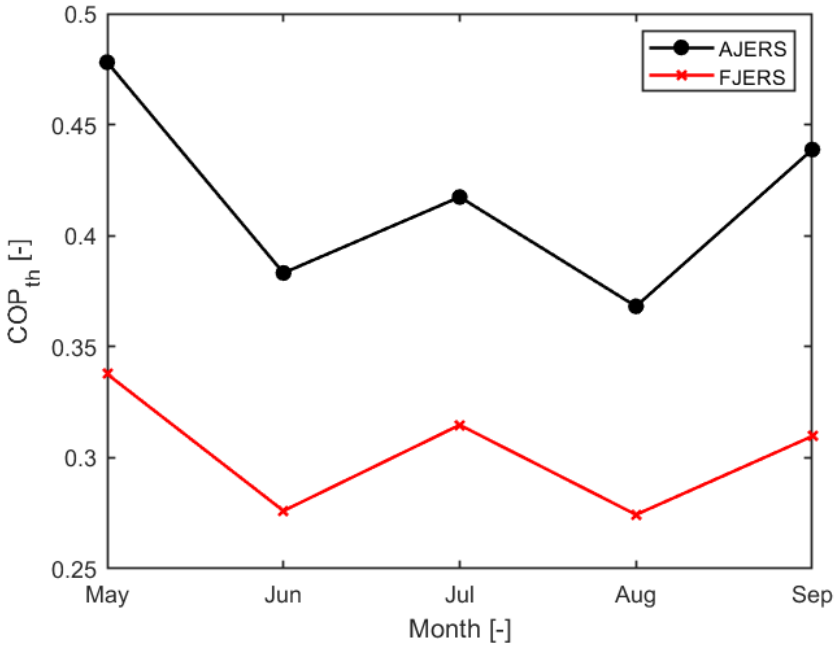

Figure 13. Monthly average COP_{th} in the warm months of the TMY

6. CONCLUSIONS

The present paper evaluates numerically the dynamic response of a solar-driven jet-ejector refrigeration system equipped with a hot thermal storage system and two different jet-ejector architectures. The first one consists of utilizing a jet-ejector with fixed geometry which is optimized to operate satisfactorily against a relatively high condensing temperature ($40\ °C$). The second one lies in a jet-ejector with an adjustable spindle that is actively controlled depending on the instantaneous condensing temperature. The conclusions obtained after analyzing the behavior of both approaches throughout the typical meteorological year of a Mediterranean latitude are outlined below.

The adjustable jet-ejector refrigeration system showed a significant improvement in all the months evaluated when compared to the fixed-geometry refrigeration system. The average COP_{th} along the month with the highest outdoor temperature (July) corresponds to 0.31 when the fixed-geometry system is used whereas the adjustable layout reaches $COP_{th} = 0.42$. The potential improvement is even greater in May and September when the average condensing temperature is normally far lower from fixed jet-ejector design condensing temperature. Indeed, in May the greatest performance difference is found. In this month, the fixed-geometry system exhibits an average $COP_{th} = 0.34$ while the adjustable system reaches a $COP_{th} = 0.48$.

The adjustable jet-ejector has demonstrated to be a useful mechanism to both extend the operational range of the refrigeration system as well as improving its performance due to its:

- Greater flexibility of the adjustable jet-ejector allowing for a smooth operation when the fixed jet-ejector critical condensing temperature is exceeded.
- More efficient management of the thermal level available in the storage tank thanks to the lower thermal power consumption when the instantaneous condensing

temperature is below its critical value. This explains its superior ability to remain in operation when the solar irradiation is insufficient.

REFERENCES

Allouche, Y., Varga, S., Bouden, C., Oliveira, A.C., 2017. Dynamic simulation of an integrated solar-driven ejector based air conditioning system with PCM cold storage. Appl. Energy 190, 600–611. https://doi.org/10.1016/j.apenergy.2017.01.001

Besagni, G., Mereu, R., Inzoli, F., 2016. Ejector refrigeration: A comprehensive review. Renew. Sustain. Energy Rev. 53, 373–407. https://doi.org/10.1016/j.rser.2015.08.059

Chen, J., Jarall, S., Havtun, H., Palm, B., 2015. A review on versatile ejector applications in refrigeration systems. Renew. Sustain. Energy Rev. 49, 67–90. https://doi.org/10.1016/j.rser.2015.04.073

Chen, W., Huang, C., Chong, D., Yan, J.J., 2019. Numerical assessment of ejector performance enhancement by means of combined adjustable-geometry and bypass methods. Appl. Therm. Eng. 149, 950–959. https://doi.org/10.1016/j.applthermaleng.2018.12.052

Chen, X., Omer, S., Worall, M., Riffat, S., 2013. Recent developments in ejector refrigeration technologies. Renew. Sustain. Energy Rev. 19, 629–651. https://doi.org/10.1016/j.rser.2012.11.028

Chen, Z., Jin, X., Dang, C., Hihara, E., 2017a. Ejector performance analysis under overall operating conditions considering adjustable nozzle structure. Int. J. Refrig. 84, 274–286. https://doi.org/10.1016/j.ijrefrig.2017.08.005

Chen, Z., Jin, X., Shimizu, A., Hihara, E., Dang, C., 2017b. Effects of the nozzle configuration on solar-powered variable geometry ejectors. Sol. Energy 150, 275–286. https://doi.org/10.1016/j.solener.2017.04.017

Dennis, M., Garzoli, K., 2011. Use of variable geometry ejector with cold store to achieve high solar fraction for solar cooling. Int. J. Refrig. 34, 1626–1632. https://doi.org/10.1016/j.ijrefrig.2010.08.006

Desideri, A., Dickes, R., Bonilla, J., Valenzuela, L., Quoilin, S., Lemort, V., 2018. Steady-state and dynamic validation of a parabolic trough collector model using the ThermoCycle Modelica library. Sol. Energy 174, 866–877. https://doi.org/10.1016/j.solener.2018.08.026

Diaconu, B.M., Varga, S., Oliveira, A.C., 2011. Numerical simulation of a solar-assisted ejector air conditioning system with cold storage. Energy 36, 1280–1291. https://doi.org/10.1016/j.energy.2010.11.015

Fasquelle, T., Falcoz, Q., Neveu, P., Lecat, F., Flamant, G., 2017. A thermal model to predict the dynamic performances of parabolic trough lines. Energy 141, 1187–1203. https://doi.org/10.1016/j.energy.2017.09.063

Galindo, J., Dolz, V., García-Cuevas, L.M., Ponce-Mora, A., 2020. Numerical evaluation of a solar-assisted jet-ejector refrigeration system: Screening of environmentally friendly refrigerants. Energy Convers. Manag. 210, 112681. https://doi.org/10.1016/j.enconman.2020.112681

García Del Valle, J., Saíz Jabardo, J.M., Castro Ruiz, F., San José Alonso, J.F., 2014. An

experimental investigation of a R-134a ejector refrigeration system. Int. J. Refrig. 46, 105–113. https://doi.org/10.1016/j.ijrefrig.2014.05.028

Gil, B., Kasperski, J., 2015. Efficiency analysis of alternative refrigerants for ejector cooling cycles. Energy Convers. Manag. 94, 12–18. https://doi.org/10.1016/j.enconman.2015.01.056

Hakkaki-Fard, A., Aidoun, Z., Ouzzane, M., 2015a. A computational methodology for ejector design and performance maximisation. Energy Convers. Manag. 105, 1291–1302. https://doi.org/10.1016/j.enconman.2015.08.070

Hakkaki-Fard, A., Poirier, M., Aidoun, Z., Ouzzane, M., Giguère, D., 2015b. An experimental study of ejectors supported by CFD. Refrig. Sci. Technol. 2030–2037. https://doi.org/10.18462/iir.icr.2015.0609

Hu, J., Shi, J., Liang, Y., Yang, Z., Chen, J., 2014. Numerical and experimental investigation on nozzle parameters for R410A ejector air conditioning system. Int. J. Refrig. 40, 338–346. https://doi.org/10.1016/j.ijrefrig.2013.12.008

Lin, C., Cai, W., Li, Y., Yan, J., Hu, Y., 2012. The characteristics of pressure recovery in an adjustable ejector multi-evaporator refrigeration system. Energy 46, 148–155. https://doi.org/10.1016/j.energy.2012.09.007

Liu, F., Groll, E.A., Li, D., 2012. Investigation on performance of variable geometry ejectors for CO2 refrigeration cycles. Energy 45, 829–839. https://doi.org/10.1016/j.energy.2012.07.008

Ma, X., Zhang, W., Omer, S.A., Riffat, S.B., 2010. Experimental investigation of a novel steam ejector refrigerator suitable for solar energy applications. Appl. Therm. Eng. 30, 1320–1325. https://doi.org/10.1016/j.applthermaleng.2010.02.011

Mazzelli, F., Milazzo, A., 2015. Performance analysis of a supersonic ejector cycle working with R245fa. Int. J. Refrig. 49, 79–92. https://doi.org/10.1016/j.ijrefrig.2014.09.020

Ministerio de Fomento (Gobierno de España), 2017. Documento Básico HE. Ahorro de energía (Código Técnico de la Edificación) 1–77.

Omidvar, A., Ghazikhani, M., Modarres Razavi, S.M.R., 2016. Entropy analysis of a solar-driven variable geometry ejector using computational fluid dynamics. Energy Convers. Manag. 119, 435–443. https://doi.org/10.1016/j.enconman.2016.03.090

Pereira, P.R., Varga, S., Soares, J., Oliveira, A.C., Lopes, A.M., De Almeida, F.G., Carneiro, J.F., 2014. Experimental results with a variable geometry ejector using R600a as working fluid. Int. J. Refrig. 46, 77–85. https://doi.org/10.1016/j.ijrefrig.2014.06.016

Pollerberg, C., Ali, A.H.H., Dötsch, C., 2009. Solar driven steam jet ejector chiller. Appl. Therm. Eng. 29, 1245–1252. https://doi.org/10.1016/j.applthermaleng.2008.06.017

Richter, M., McLinden, M.O., Lemmon, E.W., 2011. Thermodynamic properties of 2,3,3,3-tetrafluoroprop-1-ene (R1234yf): Vapor pressure and p - ϕ - T Measurements and an Equation of State. J. Chem. Eng. Data 56, 3254–3264. https://doi.org/10.1021/je200369m

Rodríguez-Hidalgo, M.C., Rodríguez-Aumente, P.A., Lecuona, A., Legrand, M., Ventas, R., 2012. Domestic hot water consumption vs. solar thermal energy storage: The optimum size of the storage tank. Appl. Energy 97, 897–906. https://doi.org/10.1016/j.apenergy.2011.12.088

Shestopalov, K.O., Huang, B.J., Petrenko, V.O., Volovyk, O.S., 2015. Investigation of an

experimental ejector refrigeration machine operating with refrigerant R245fa at design and off-design working conditions. Part 2. Theoretical and experimental results. Int. J. Refrig. 55, 212–223. https://doi.org/10.1016/j.ijrefrig.2015.02.004

Tashtoush, B., Alshare, A., Al-Rifai, S., 2015. Hourly dynamic simulation of solar ejector cooling system using TRNSYS for Jordanian climate. Energy Convers. Manag. 100, 288–299. https://doi.org/10.1016/j.enconman.2015.05.010

Varga, S., Lebre, P.M.S., Oliveira, A.C., 2013. CFD study of a variable area ratio ejector using R600a and R152a refrigerants. Int. J. Refrig. 36, 157–165. https://doi.org/10.1016/j.ijrefrig.2012.10.016

Varga, S., Oliveira, A.C., Ma, X., Omer, S.A., Zhang, W., Riffat, S.B., 2011. Experimental and numerical analysis of a variable area ratio steam ejector. Int. J. Refrig. 34, 1668–1675. https://doi.org/10.1016/j.ijrefrig.2010.12.020

Varga, S., Oliveira, A.C., Palmero-Marrero, A., Vrba, J., 2017. Preliminary experimental results with a solar driven ejector air conditioner in Portugal. Renew. Energy 109, 83–92. https://doi.org/10.1016/j.renene.2017.03.016

Wang, L., Liu, J., Zou, T., Du, J., Jia, F., 2018. Auto-tuning ejector for refrigeration system. Energy 161, 536–543. https://doi.org/10.1016/j.energy.2018.07.110

Yen, R.H., Huang, B.J., Chen, C.Y., Shiu, T.Y., Cheng, C.W., Chen, S.S., Shestopalov, K., 2013. Performance optimization for a variable throat ejector in a solar refrigeration system. Int. J. Refrig. 36, 1512–1520. https://doi.org/10.1016/j.ijrefrig.2013.04.005

Zaversky, F., García-Barberena, J., Sánchez, M., Astrain, D., 2013. Transient molten salt two-tank thermal storage modeling for CSP performance simulations. Sol. Energy 93, 294–311. https://doi.org/10.1016/j.solener.2013.02.034